applied sciences

MDPI

Article

Mechanisms of Sweep on the Performance of Transonic Centrifugal Compressor Impellers

Xiao He and Xinqian Zheng *

Turbomachinery Laboratory, State Key Laboratory of Automotive Safety and Energy, Tsinghua University, Beijing 100084, China; hex15@mails.tsinghua.edu.cn

* Correspondence: zhengxq@tsinghua.edu.cn; Tel.: +86-10-6279-2333

Received: 17 August 2017; Accepted: 12 October 2017; Published: 18 October 2017

Featured Application: The mechanism for the optimal sweep angle of centrifugal compressors has been proposed, which benefits high-efficiency designs of centrifugal compressors for turbocharger and gas turbine engine applications.

Abstract: Transonic centrifugal compressors with high performance are required in the oil and gas industries, modern gas turbine engines, and turbochargers. The sweep of the blades is one of the crucial features that have a significant influence on their performance. This paper numerically investigates mechanisms by which sweep affects the performance of a transonic impeller with twin splitters. Sweep is defined as scaling up or down the shroud chord, and the variation range of the sweep angle has been chosen from −25 to +25°. In the current case, results show that the variation of choke mass flow rate, pressure ratio, and efficiency value is around 1%. If the centrifugal compressor has a higher pressure ratio or a higher front loading, the sweep effect on compressor performance will be even stronger. The essential aerodynamic effect of sweep is the spanwise redistribution of the front loading, resulting in effects on the shock structure, the tip leakage vortex, and the flow separation. On the shroud section, forward sweep restricts the front loading, the shock strength, and the tip leakage vortex, which reduces the loss near the casing. On the hub section, aft sweep suppresses the front loading and the flow separation, which reduces the loss near the hub. It is the delicate balance between controlling the loss near the hub and the loss near the casing that determines the optimal sweep angle design.

Keywords: centrifugal compressor; shock wave; flow control

1. Introduction

Centrifugal compressors are widely applied in the oil and gas industries [1,2], gas turbine engines, and [3–5] turbochargers [6,7]. In the aviation industry, transonic centrifugal compressors with a high pressure ratio are required for reduction of manufacturing costs and engine weight. In the automotive industry, the tendency towards downsizing and emissions control in internal combustion engines favors the use of turbochargers with centrifugal compressors of both high pressure ratio and efficiency. One of the prime elements for performance improvement of centrifugal compressors is the impeller. For impellers with tip gaps, the greatest source of loss generation comes from the tip leakage flow [8]. When a shock wave occurs under transonic inlet conditions, the interaction of the shock wave, the boundary layer and tip leakage vortex will further deteriorate the complex flowfield as well as the performance of transonic impellers [9].

Sweep is a degree of freedom of the blade stacking style. When the shroud section of the blade extends upstream in the chord line direction (or axial direction), it is defined as forward sweep. The opposite is regarded as aft sweep. Because the tip geometry changes with the sweep feature, impacts on the tip leakage flow and the shock structure are expected. It is therefore considered a potential way to improve the performance of modern turbomachinery.

In axial turbomachines, swept blade design has been studied for over half a century. Its application has been widely spread from compressors to turbines and from rotors to stators [10], especially applied to blade ends to improve the endwall flowfields [11]. For compressor rotors, a detailed survey [12] suggested that forward swept blades improved the efficiency and extended the stall-free operating range by reducing the near-wall and tip clearance losses, as well as controlling the secondary flows and radial migration of high-loss fluid. More recently, Okui et al. [13] optimized the sweep feature, the camber line and the chord length of a transonic axial compressor rotor. The best result in terms of efficiency and stall margin appeared to be aft-swept in combination with an S-shaped camber line and an increased chord length. For compressor fans, Vad [14] concluded that the application of forward sweep in fans with the controlled vortex design concept not only reduces the near-tip loss via moderation of the already intensified radial migration of low-momentum flow, but also decreases the friction loss away from the endwalls by shortening the already elongated flow path. Different designs of forward sweep and aft sweep in a fan with the controlled vortex design concept were examined later by Ilikan and Ayder [15]. The enlarging forward sweep angle appeared to improve the performance especially in low mass flow operating conditions. With regard to transonic axial compressors with shocks, the sweep feature also has a significant effect on the shock structure. Hah et al. [16] concluded that the passage shock would move relatively downstream in the forward sweep design, and vice versa for the aft sweep case. The forward sweep was found to improve both the efficiency and the stall margin. Similar trend of the shock front movement and the efficiency increment was captured in the Rotor 37 case [17,18]. Denton and Xu [19] applied sweep to a transonic fan, where the stall margin was significantly extended due to the optimized shock structure. URANS and LES methods were recently applied by Hah and Shin [20] to investigate the near-stall flow mechanism of a transonic fan. It is shown that a compound sweep design enabled the passage shock to stay near the leading edge rather than to detach from the blade, which resulted in a much more stable flow structure near the tip region.

Among all swept axial cases, it is generally found that the stall margin will be improved by forward sweep and vice versa. Most designs with forward sweep showed better efficiency than that of the unswept or the aft-swept ones. Nevertheless, cases do exist that aft sweep also has the potential to improve the efficiency [21].

In radial turbomachines, although there are applications of sweep to reduce the stress levels [22], control the blade root separations [23], and adjust the flow capacity [24], a parametric study of sweep has relatively seldom been reported. When sweep is applied to the impeller main blade, similar effects on the flowfield are expected because the local flow patterns of the axial part of the impeller are much similar to that of the axial compressors. Hazby and Xu [25] confirmed the aerodynamic effects of the main blade sweep on controlling the leading edge loading, the shock structure and the accumulation of low-momentum flow in a turbocharger impeller case. It was found that an increase in sweep angle led to an increased efficiency due to the weaker shock-boundary layer and shock-leakage interaction loss. Later, the numerical results of Erdmenger and Michelassi [26] implied that forward sweep only increased the stable operating range while aft sweep increased the efficiency. When sweep is applied to splitters, its effects remain uncertain because its leading edge locates further downstream, where the local flow patterns are much more complex than that of the main blade. Cases with swept splitters and unswept main blades were reported by Hazby and Xu [27]. The impact on the aerodynamic performance was comparatively limited, and the aerodynamic effects on the flowfield have not been well understood. Because of limited studies of impeller sweep, there are still some remaining questions listed as follows:

1. The impacts of blade sweep on the aerodynamic performance of the centrifugal impeller have not been systematically studied yet. It is hard to tell the general trend of aerodynamic performance parameters (i.e., choke mass flow rate, efficiency and pressure ratio) with changing sweep feature. Such understandings are important to guide future optimization designs.
2. The aerodynamic effects of sweep on the flowfield have not been fully understood. Some of the effects in the axial part of the impeller were reported in previous research, but few

studies have addressed the axial-to-radial part of the impeller, which differs between axial and radial turbomachines.

3. The underlying mechanism for the optimal sweep angle with best efficiency has not yet been determined.

To answer these remaining questions, mechanisms of sweep on the aerodynamic performance of a transonic impeller with twin splitters have been numerically investigated in this paper. Sweep is defined as scaling up or down the shroud chord while keeping the blade angle and the thickness distribution along the relative chord length unchanged. The variation range of the sweep angle has been chosen from -25° to $+25^\circ$. Performances of both datum and swept cases have been compared in detail, and then aerodynamic effects of sweep have been analyzed and discussed.

2. Case Description

2.1. Datum Impeller

The investigated transonic impeller with twin splitters is a component of a commercial small gas turbine engine. The impeller is illustrated in Figure 1, and its main specification is given in Table 1. The leading edge of the main blade is designed aft-swept (-21° of sweep angle) for stress considerations, and that of splitter I and splitter II is unswept. The trailing edges of all blades are axial stacking. A vaned diffuser and a bent pipe are attached to the impeller downstream. However, in order to avoid the issue of stage matching, the calculation domain of swept cases only includes the impeller and an extended vaneless region.

Figure 1. Datum impeller.

Table 1. Main specifications of datum impeller.

Parameters	Symbols	Values
Number of blades	Z	13 + 13 + 13
Normalized leading edge hub radius	r_{1h}/r_2	0.41
Normalized leading edge tip radius	r_{1t}/r_2	0.56
Normalized exit blade height	b_2/r_2	0.05
Pressure ratio	π	3.0
Flow coefficient	ϕ	0.05
Pressure coefficient	ψ	0.68
Specific speed	N_s	0.60

2.2. Sweep Definition

In axial cases, sweep can be defined as moving the shroud section parallel along the axial or chord direction and keeping the chord length unchanged [19]. However, the definition of sweep in centrifugal impellers cannot be directly inherited from that of the axial cases. Otherwise, the trailing edge radius and the work input of the centrifugal compressor will be greatly influenced. There are

two types of sweep definition in centrifugal impellers. The first one is to cut or to extend the tip of the leading edge along the chord direction while maintaining the rest part unchanged [25], as showed in Figure 2a. The second definition is to adjust the tip of the leading edge by scaling up or down the shroud chord while keeping the blade angle and thickness distribution along the relative chord length unchanged, as illustrated in Figure 2b. Because the second definition allows the sweep feature to be independent from blade angle and thickness distributions, it is more practical when coupling with optimization techniques. Therefore, the second definition is adopted in this study.

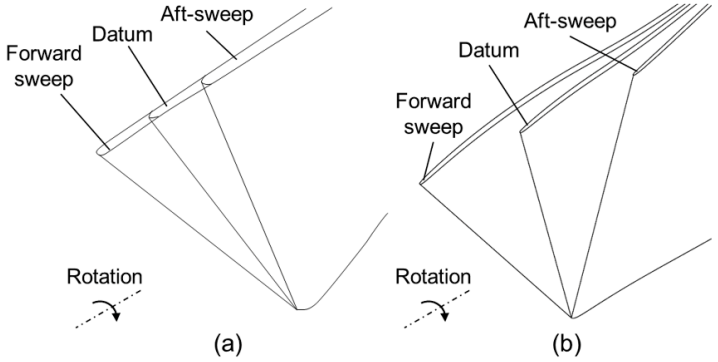

Figure 2. Sweep definition: (**a**) maintaining rest blade part and (**b**) maintaining relative blade angle and thickness distribution.

To quantitatively define the extent of sweep, the sweep angle between the leading edge trace and the radial direction is adopted, as illustrated in Figure 3a. A positive value of sweep angle represents forward sweep, and the opposite is aft sweep. During the parametric study, the sweep definition of twin splitters is inherited from the main blade, where the camber line of the main blade is truncated to define the splitters with respect to the unchanged relative meridional position of the splitter leading edge. In other words, when the sweep angle of the main blade changes, both splitters will change in similar fashion, as presented in Figure 3b. Through this simplified approach, sweep features of all blades can be defined by only one parameter, while sweep effects on impeller performance and flowfields can still be well estimated and captured. For a real impeller optimal design process, it is necessary to decouple the sweep design of different blades. The investigated variation range of the sweep angle of main blade has been chosen from −25° to +25°, which covers most of the swept impeller designs in earlier researches.

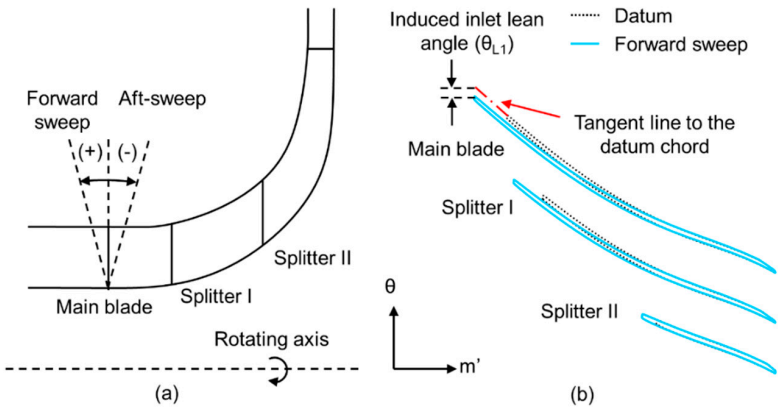

Figure 3. Swept geometry: (**a**) meridional view and (**b**) shroud sections of all blades.

Admittedly, the current definition of sweep will introduce extra lean. It is shown in Figure 3b that an extra lean will be introduced from the mid-chord to the leading edge of the main blade, while the

exit lean angle (or rake angle) is remained the same. The ratio of the change in lean angle to that in sweep angle has been analyzed to be only −13% in this case (Appendix A). Because such extent of blade lean at axial part of the impeller has limited effect on impeller efficiency [28] and flowfields [29], it is neglected except for the choke analysis.

3. Numerical Method and Validation

3.1. Numerical Method

The simulation by computational fluid dynamics (CFD) is done with the solver EURANUS based on a three-dimensional steady, compressible, finite volume scheme to solve the Reynolds-averaged Navier–Stokes equations in the conservative formulation. To receive a credible viscosity resolution, spatial discretization is achieved with a modified Jameson central difference scheme. The fourth-order Runge–Kutta scheme is applied for temporal discretization. The convergence of the solver is accelerated by the multigrid procedure.

Several turbulence models have been successfully applied to compressors. Near peak efficiency conditions, because the major flow phenomena (tip leakage flows, secondary flows and shock waves) are not essentially driven by viscosity, the basic physics can be well represented by simple turbulence models or even by the inviscid Euler equations [30]. Near surge conditions, significant differences between turbulence models occur because the predicted fully separated flow in blade passages is highly depended on the modeled turbulent viscosity, but there seems to be no universal turbulence model that is always superior to others [31]. Assessment of turbulence models in centrifugal compressors were carried out in the SRV2-O case [32] and the Radiver case [33]. It is generally found that the Spalart–Allamaras model, the k-ω shear stress transport model, the v^2-f-k-ε Durbin model and the Reynolds stress model can predict very similar flow features at the impeller peak efficiency condition, but the Spalart–Allamaras model has limitations in vaned diffuser flow fields where the fully separated flow is dominate. Considering both the accuracy for the impeller peak-efficiency flows and the calculation time, the Spalart–Allamaras one-equation model [34] is adopted.

A multi-block structured grid is built to mesh the impeller. For the O4H topology of the impeller, it consists of 153, 69, and 43 nodes in the streamwise, spanwise, and pitchwise direction, respectively. The tip clearances of all blades are set constant to 4.4% of exit blade height. To predict a boundary layer resolution sufficiently fine for the Spalart–Allamaras model, a value of 0.001 mm is found appropriate for the first layer wall distance of the near-wall grid. The resulting local normalized wall distance y+ varies from 0 to 3. All fluid domains are calculated in the rotating reference frame, and thus no rotor–stator interfaces are needed. The final grid of the datum impeller has 2.3 million volume cells for single pitch, including around 0.2 million volume cells in tip gap regions. The final grid is shown in detail in Figure 4.

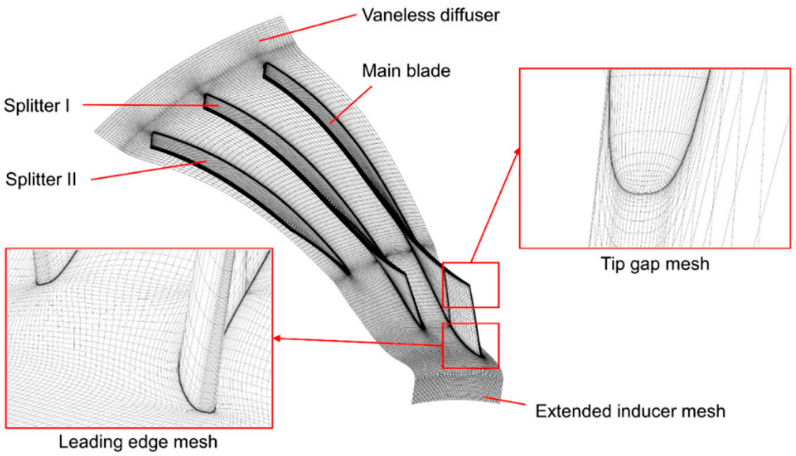

Figure 4. Created computational mesh in detail.

Total pressure, total temperature, and axial velocity direction are imposed at the inlet, and an average static pressure is imposed at the exit. The blades and casing surface are defined as rotational non-slip solid boundary and static non-slip solid boundary, respectively. For each rotation speed, the initial solution of the first simulation case is defined by estimation of velocity components, static pressure and static temperature for the whole domain. The former converged result is then used as the initial solution for the next case with higher backpressure. The step rise in backpressure at the near-surge condition is kept as 1 kPa. If no signs of numerical instabilities occur after 10,000 iterations, the solution is considered to have reached convergence.

3.2. Grid Independence Study

The accuracy of CFD results is associated with the grid size; therefore, the grid independence is studied before large amounts of simulations are carried out. Four different types of mesh within the impeller are investigated, whose number of nodes vary from 1.0 million up to 2.6 million. The resulting performance of all meshes at design speed is plotted in Figure 5a. It is illustrated that the CFD simulation produces consistent results when the mesh nodes surpass 1.5 million. In Figure 5b, the spanwise distribution of static pressure is compared at impeller exit, where all the cases share the same mass flow rate at the peak efficiency condition. The pressure distribution is reproduced for a mesh size of 2.3 million nodes and above, where the maximum difference of static pressure is only 0.03% of the backpressure. Hence, the numerical method that adopts a mesh with 2.3 million nodes is independent of the mesh resolution.

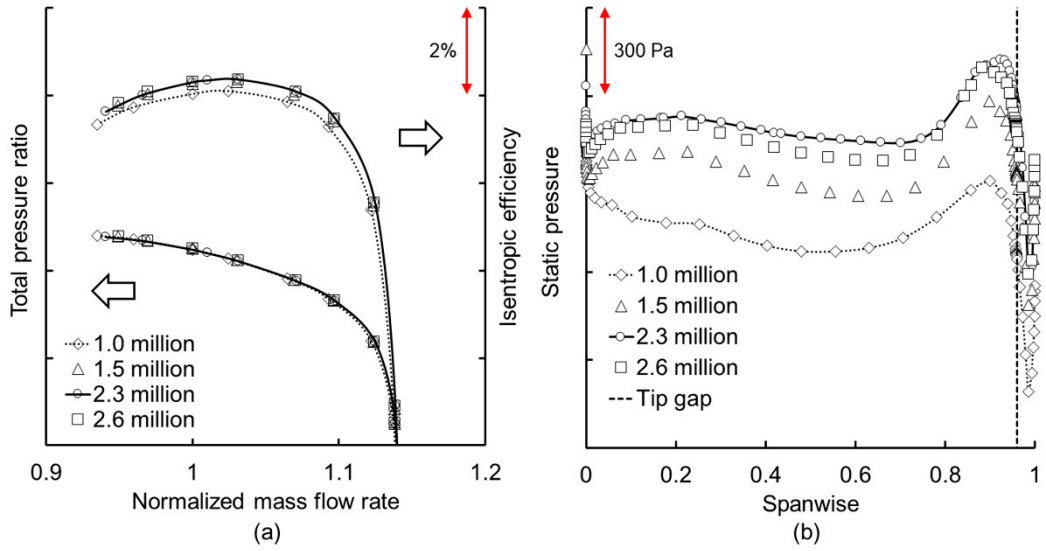

Figure 5. Grid independence: (**a**) performance at design speed and (**b**) spanwise distribution of static pressure at impeller exit, peak efficiency condition at design speed.

3.3. Validation

The rig tests of the datum compressor stage have been carried out to validate the performance prediction of CFD. Schematic of the compressor test sections is illustrated in Figure 6, where section A and B represents compressor inlet and exit test section, respectively. The CFD calculation domain for validations is also set between section A and B.

The characteristics of the datum compressor obtained from experiments and CFD are showed in Figure 7. To represent the maximum discrepancy among different tests on the same compressor, error bars are plotted in the experiment performance lines. The satisfactory agreement is obtained with respect to the choking flow prediction and the tendency of pressure curves, although there is inconsistency for surge point prediction. In this steady case, the surge point is defined as the converged point with the highest backpressure. However, it is misleading to deduce the time-dependent system

oscillations from numerical steady-state instabilities. Moreover, the application of a rotor-stator interface model will influence surge point prediction as well. At the design speed of the datum compressor stage, instability is initiated from the vaned diffuser part. Since the mixing plane model is applied to the radial gap between the impeller and the vaned diffuser, the incoming flow condition of the vaned diffuser will be different from reality, which then introduces errors in surge prediction. At 95% design speed, because the origin of instability will be shifted from the vaned diffuser to the impeller when decreasing the operating speed [35], the impact of the mixing plane model will be reduced, and thus the discrepancy on surge point prediction will also be decreased. To avoid the impeller–diffuser matching issue as well as the application of a rotor-stator interface model, only the datum impeller attached with an extended vaneless diffuser is considered in the following research.

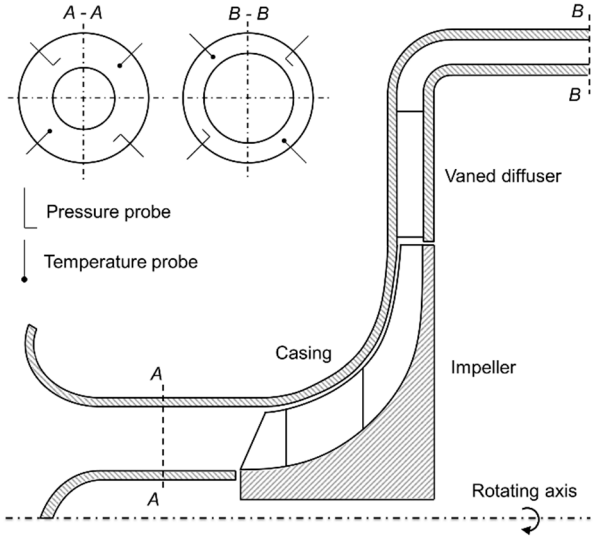

Figure 6. Schematic of compressor test sections.

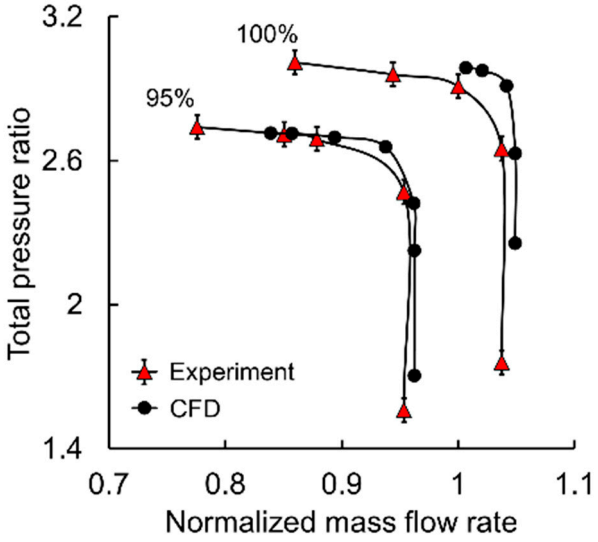

Figure 7. Comparison of pressure ratio of the datum impeller with vaned diffuser. CFD: computational fluid dynamics.

To further validate the numerical method for predicting performances and detailed flow fields of impellers with vaneless diffusers, the open transonic centrifugal compressor SRV2-O has been investigated applying the same numerical method. Its geometry specification has been given by

Eisenlohr et al. [36] and its measurement results have been provided by Krain et al. [37]. The compared pressure curves are at 60%, 70% and 80% of design speeds, where the operating pressure ratios are similar to the investigated case. The compared flow field is taking from the m/m_c = 0.89 operating point at design speed, where a strong shock wave occurs at the leading edge of the main blade. Figure 8a compares pressure curves of the SRV2-O compressor between experiments and CFD, where the CFD results agree well with the experiments. The comparison of relative Mach number near the inlet and the exit respectively is presented in Figure 8b. It is illustrated that both the shock position and the shock strength have been well captured at the tip section. The numerical method is therefore considered capable of predicting the compressor performance and the flow details near the peak efficiency condition, which is sufficient for the following discussions.

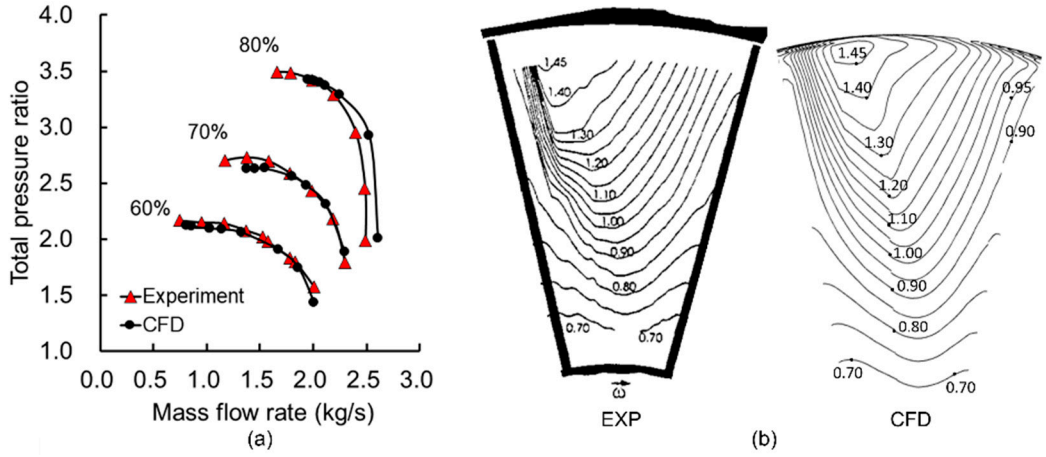

Figure 8. Comparison of (**a**) pressure ratio and (**b**) relative Mach number near the inlet of SRV2-O. EXP: experiments.

4. Performance Comparison

The aerodynamic performance parameters of a compressor include the choke mass flow rate, the efficiency, the pressure ratio and the surge margin. Because of the limitation of steady simulations, the surge margin is not analyzed in this work. In the following part, the change of other performance parameters with different sweep angle will be discussed respectively. Comparisons between cases with different sweep angle are done at the design mass flow rate, where the normalized mass flow rate m/md equals unity.

4.1. Choke Mass Flow Rate

The choke mass flow rate of cases with different sweep angle is illustrated in Figure 9. It is observed that both forward sweep and aft sweep tend to increase the flow capacity, and the variation of the choke mass flow rate is 0.8% of that of the datum case. The choke flow capacity is decided by the throat area and the blockage factor. Because of the complexity of the investigated case with twin splitters, the impeller throat area is strongly three-dimensional and its variation trend can be well captured through inviscid simulations. By comparing the choke prediction through viscid and inviscid methods, it can be concluded that the change of the throat area rather than the blockage is dominant for the trend of choke mass flow rate. When the sweep angle decreases from 0° to −25°, the throat area will be generally enlarged due to the reduced space occupied by blades at upper spans. When the sweep angle increases from 0° to +25°, the induced inlet lean angle plays a more important role that turns the throat surface more perpendicular to the axial direction, and thus increases the throat area.

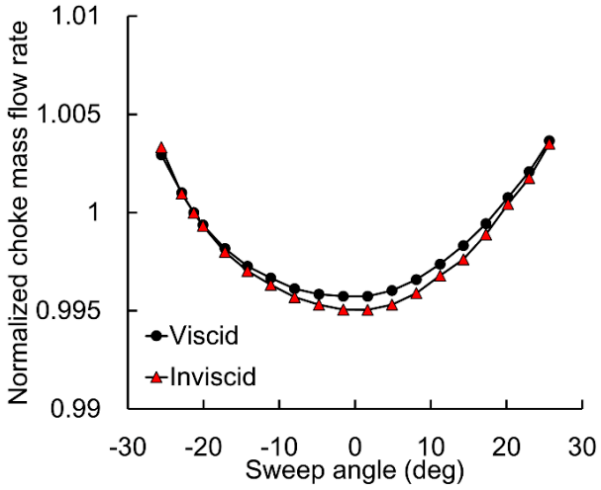

Figure 9. Choke mass flow rate of cases with different sweep angle.

4.2. Efficiency

The CFD results of efficiency with different sweep angle are presented in Figure 10a. When the sweep angle is gradually enlarged from −25° to +11°, the efficiency tends to be increased by 1.2%. The efficiency decreases moderately by 0.2% when the sweep angle further increases from +11° to +25°. The optimal sweep angle at +11° and the maximum sweep angle at +25° are referred as OSA (optimal sweep angle) and MSA (maximum sweep angle) respectively. The resulting design speed efficiency comparison between datum, OSA and MSA cases is presented in Figure 10b. It is observed that a 0.8% increase in efficiency occurs at the whole speed line of OSA. The high mass flow conditions of MSA are similar to OSA, but a deficit of 0.2% in efficiency occurs at low mass flow conditions.

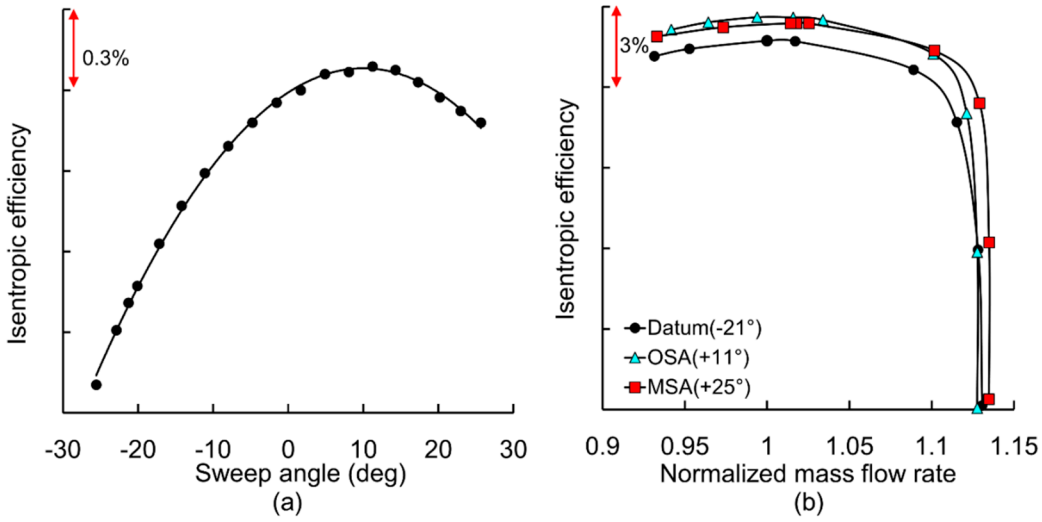

Figure 10. Efficiency: (**a**) trend with sweep angle and (**b**) design speed performance comparison. OSA: optimal sweep angle; MSA: maximum sweep angle.

For the purpose of understanding the loss reduction in detail, the parameter efficiency deviation ($\Delta\eta$) is applied to investigate the loss reduction process, which is defined based on the concept of loss of efficiency [38]:

$$\Delta\eta(M) = \left(\frac{T_{02}\Delta s(M)}{\Delta h_{02}}\right)\Big|_{sweep}^{datum} \quad (1)$$

$$\Delta\eta(N) = \left(\frac{T_{02}\Delta s(N)}{\Delta h_{02}}\right)\Big|_{sweep}^{datum}, \tag{2}$$

where M and N are the corrected streamwise and spanwise coordinates from 0 to 1 (inlet to exit and hub to shroud), respectively, $\Delta s(M)$ is the mass-averaged entropy rise of a cross-section cut at certain streamwise position, and $\Delta s(N)$ is the pitch-averaged entropy rise at a certain spanwise position of a cross-section cut. The increase of $\Delta\eta$ along the streamwise direction represents loss reduction at a corresponding location, and a positive value of $\Delta\eta$ along the spanwise direction represents a higher efficiency at a corresponding location.

The streamwise $\Delta\eta$ distribution of OSA and MSA cases is shown in Figure 11. From inlet to Section I near the leading edge of splitter I, $\Delta\eta$ drops suddenly at first and finally increases quickly. The sudden changes of $\Delta\eta$ are caused by the sweep of main blade leading edge, where the incoming flow encounters the leading edge and generates entropy at a more upstream location. The negative value of $\Delta\eta$ at Section I is due to additional friction loss by the increased blade surface area. Comparing OSA with MSA, it is illustrated that the too large sweep angle induces extra loss near Section I, which is responsible for the efficiency drop from +11° to +25° of sweep angle. From Section I to Section II near the leading edge of splitter II, $\Delta\eta$ increases gradually. From Section II to the exit, $\Delta\eta$ increases at a much higher rate. Generally, the efficiency improvement focuses near the radial part of the impeller, although the blade modification by sweep is made near the axial part.

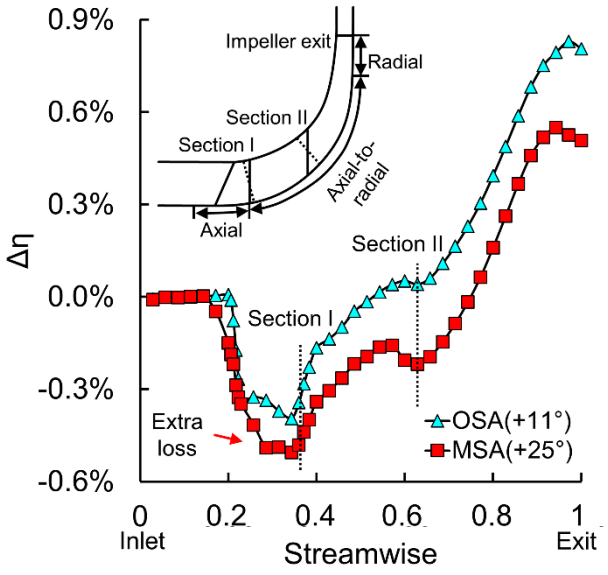

Figure 11. Streamwise efficiency deviation distribution.

The pitch-averaged spanwise $\Delta\eta$ distribution at Section I and the impeller exit is illustrated in Figure 12. At Section I in Figure 12a, it is observed that the induced extra loss from OSA to MSA occurs near the hub, where the $\Delta\eta$ of MSA is obviously lower than that of OSA. At impeller exit in Figure 12b, it can be seen that the efficiency significantly improves near the casing in both case. When increasing sweep angle from OSA to MSA, the loss near the casing is further reduced, but the loss near the hub is enhanced. The trade-off effect determines the best sweep angle in terms of efficiency. To pinpoint the trade-off effect, $\Delta\eta$ contour of both cases at impeller exit is presented, where the change of $\Delta\eta$ focus on passages around the main blade.

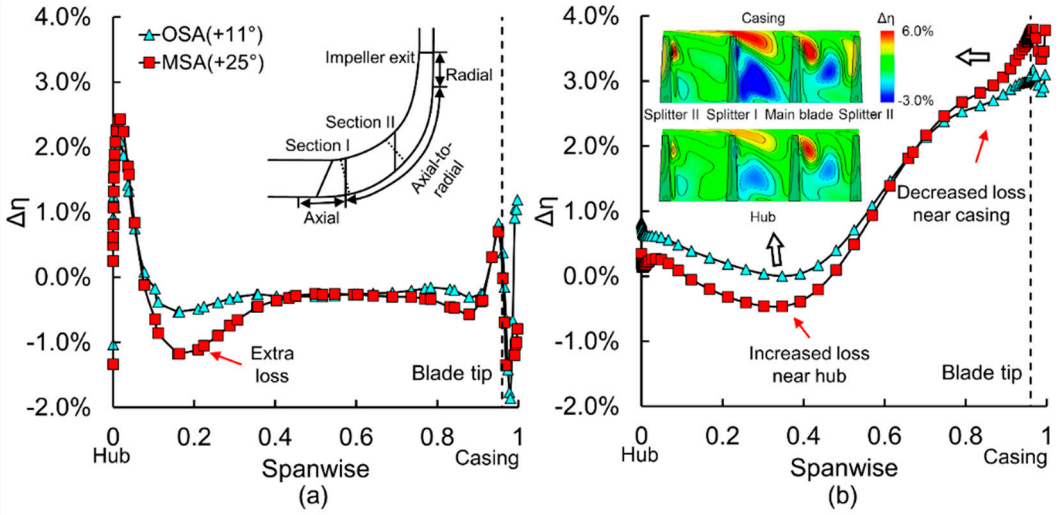

Figure 12. Spanwise pitch-averaged efficiency deviation distribution at (**a**) Section I and (**b**) impeller exit.

4.3. Pressure Ratio

The pressure ratio of cases with different sweep angle is illustrated in Figure 13a. It is shown that the highest pressure ratio also occurs at the optimal sweep angle. The variation range of the pressure ratio is 1.2% of that of the datum case. Despite the lowered efficiency of other cases, the total temperature ratio, which can be used to evaluate the change of work input, is also examined in Figure 13a. The variation of the total temperature ratio is less than 0.2% of that of the datum case, which implies that the work input is barely changed by sweep. The work input will only be influenced by the blade turning angle and the slip factor. Since the blade angle distribution and the rear part of the impeller have been kept unchanged, barely changes are expected in both the blade turning angle and the slip factor, and thus the work input. The resulting design speed pressure ratio comparison between datum, OSA and MSA cases is presented in Figure 13b, where the change of pressure ratio is limited due to the relatively small change in efficiency and the nearly unchanged work input.

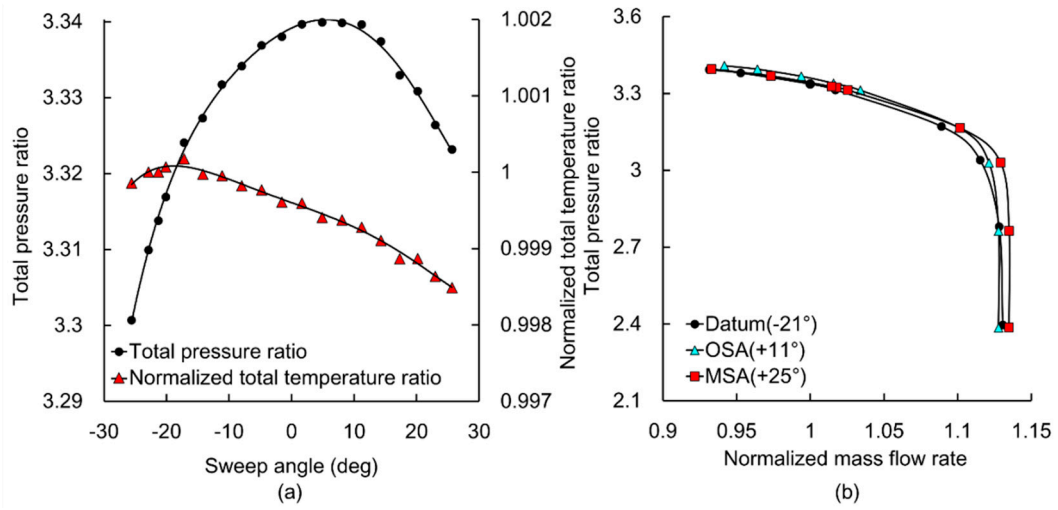

Figure 13. Pressure ratio: (**a**) trend with sweep angle and (**b**) design speed performance comparison.

5. Aerodynamic Effects of Sweep Feature

5.1. Effect on the Front Loading

The effect of sweep on the front loading of main blade can be observed in Figure 14. It is illustrated that the front loading near the tip is decreased with the enlarged sweep angle, while that near the hub is increased. Because the front of main blade locates at the axial part of the impeller, the loading redistribution effect is similar with that in the axial case [12]. Such effect is also reported in a former centrifugal case [25], but the extent in the current case is much stronger due to the significant change of sweep angle. The effect of sweep on the front loading of splitters is also examined in Figure 15. For splitter I, both the front loading near the hub and the tip has been decreased. While for splitter II, the front loading near the tip has been slightly decreased, and that near the hub has been increased. The effect on the front loading of splitters is therefore different from the main blade.

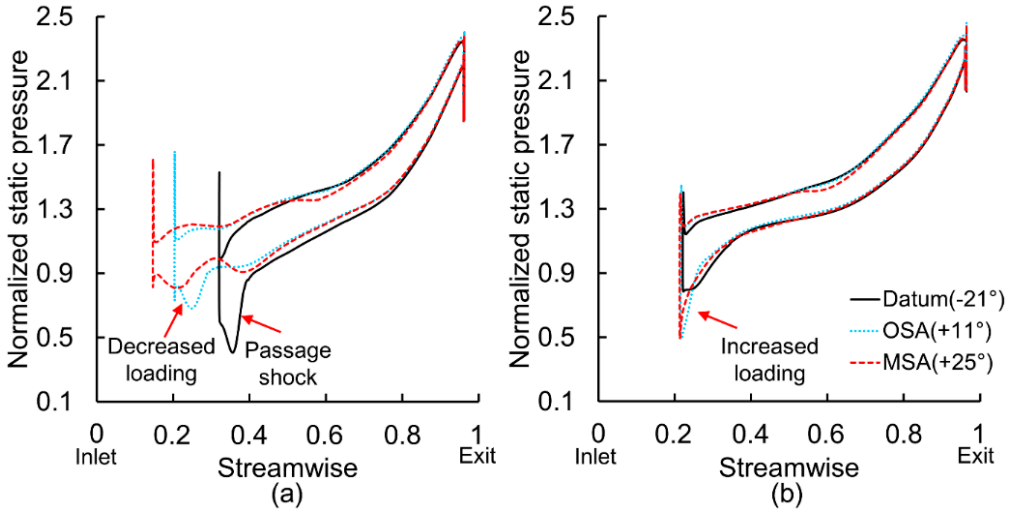

Figure 14. Static pressure distribution of main blade at (**a**) 95% span and (**b**) 5% span.

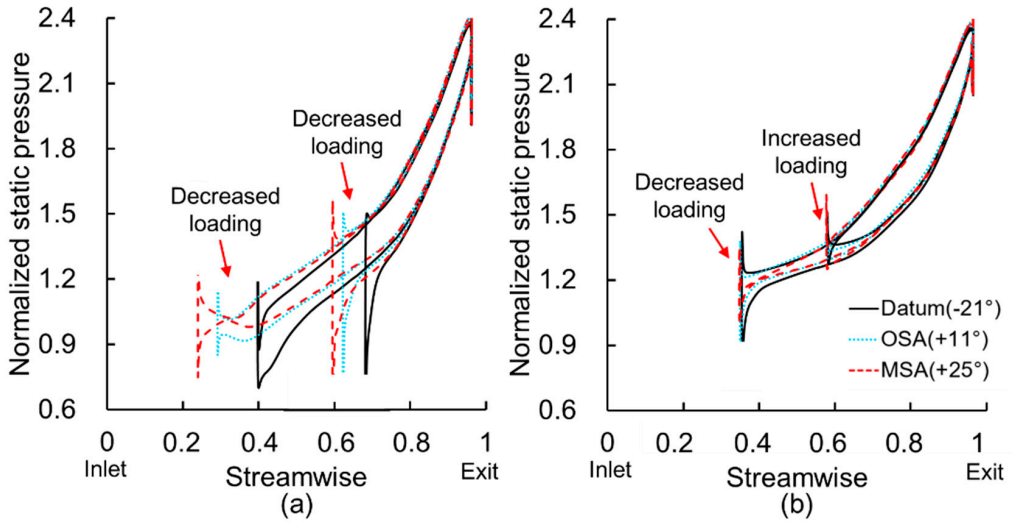

Figure 15. Static pressure distribution of splitters at (**a**) 95% span and (**b**) 5% span.

To understand sweep effects on the front loading of different blades, one of the explanations is given based on the streamline twist. For axial turbomachines and axial parts of centrifugal compressors, illustration of streamlines is shown in Figure 16a. When the blade is designed aft-swept, a secondary

flow that drives the fluid from the pressure side (PS) across the leading edge to the suction side (SS) exist, which works in similar fashion with the tip leakage flow. The leading edge secondary flow is generated by the local pressure gradient, where the incoming flow pressure is lower than the pressure side pressure and higher than the suction side pressure near the leading edge. As a result, the suction side and pressure side streamline will be twisted radially inward and outward, respectively. The axial velocity at suction side near the hub will therefore be higher, which leads to a lower incidence and a decreased loading. The axial velocity at suction side near the tip will be lower, which results in a higher incidence and an increased loading. When the blade is designed forward swept, it can be deduced in a similar manner that the front loading near the hub will be increased, while that near the tip will be decreased.

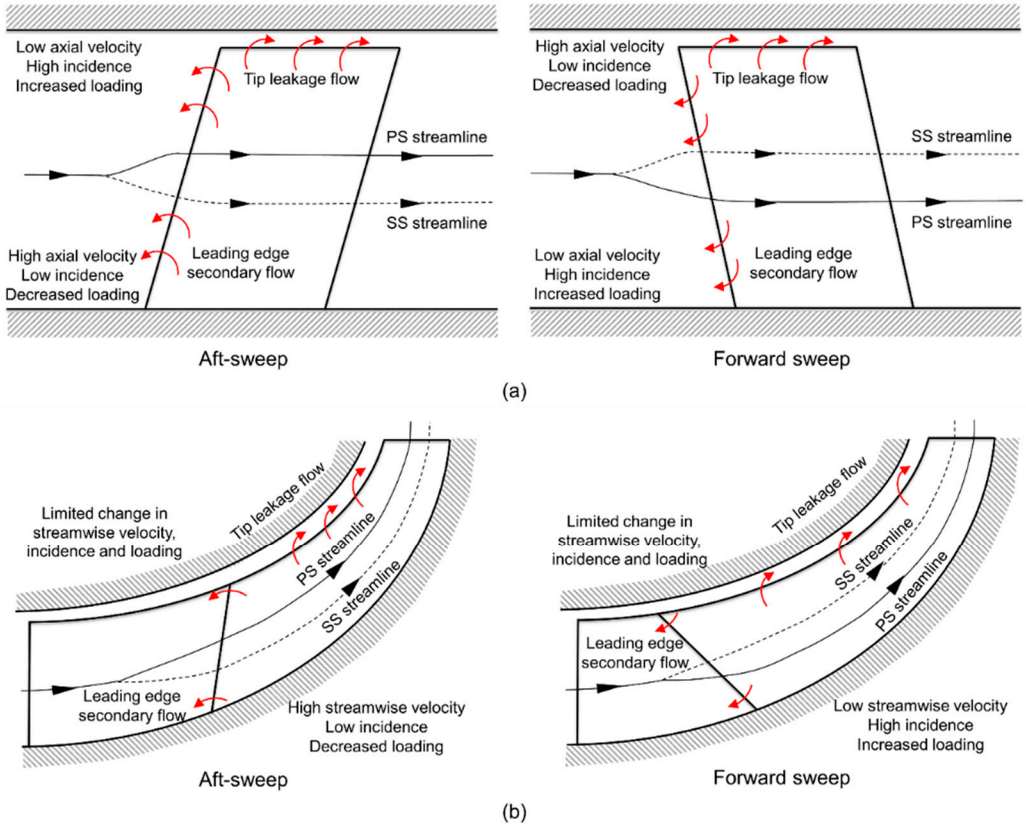

Figure 16. Understanding sweep effects on the front loading of (**a**) axial compressors and (**b**) centrifugal compressors through streamline twist.

For axial-to-radial parts of centrifugal compressors, the streamline twist also exists as illustrated in Figure 16b. For the front loading near the hub, similar conclusion is obtained due to the streamline twist effect. For the front loading near the tip, however, the tip incidence is also altered through the incoming flow swirl. When increasing the sweep angle, the blade tip encounters flow more upstream with a higher relative flow angle, which tends to increase the incidence and the loading near the tip, and thus counteracts with the streamline twist effect. Therefore, limited change in streamwise velocity, incidence and loading is obtained near the tip. It should be noted that the above incoming flow swirl pattern is only true when there are blades upstream, which gradually turns the flow from high relative flow angle at inlet to low relative flow angle at exit. This is the case for most impellers with splitters.

Another approach to understand sweep effects on front loading is based on the loading definition, which is the pressure difference between pressure side and suction side of the blade. For axial turbomachines and axial part of centrifugal impellers, illustration of loading is shown in Figure 17a. The front loading at the blade tip (point A and A') can be expressed by the loading perpendicular away from the tip (point B and B') with an integral term:

$$\lambda_A = \lambda_B + \int_{r_B}^{r_A} \frac{\partial \lambda}{\partial r} dr \tag{3}$$

$$\lambda_{A'} = \lambda_{B'} + \int_{r_{B'}}^{r_{A'}} \frac{\partial \lambda}{\partial r} dr. \tag{4}$$

Because the radial gradient of blade loading is decided by the radial gradient of pressure, it can be deduced from the radial equivalent equation:

$$F_r + \frac{V_t^2}{r} = V_x \frac{\partial V_r}{\partial x} + V_r \frac{\partial V_r}{\partial r} + \frac{1}{\rho} \frac{\partial p}{\partial r}, \tag{5}$$

where terms on the left hand side represent the radial blade force and the centrifugal force respectively, while terms on the right hand side represent the radial inertial force and the pressure gradient respectively. For simplicity, the radial blade force is ignored because it is usually introduced by blade lean. The radial velocity is usually much smaller than the other two components, and its axial gradient is also considered small. Equation (5) is then simplified into the equation of simple radial equilibrium:

$$\frac{\partial p}{\partial r} = \rho \frac{V_t^2}{r}. \tag{6}$$

Therefore, the radial gradient of blade loading is obtained:

$$\frac{\partial \lambda}{\partial r} = -\rho \frac{V_{t,s}^2 - V_{t,p}^2}{r}. \tag{7}$$

Equation (7) reveals that the loading gradient mainly depends on the tangential velocity of the incoming flow, which does not change with the sweep angle. Comparing Equations (3) and Equations (4):

$$\lambda_A - \lambda_B = \int_{r_B}^{r_A} \frac{\partial \lambda}{\partial r} dr \approx \int_{r_{B'}}^{r_{A'}} \frac{\partial \lambda}{\partial r} dr = \lambda_{A'} - \lambda_{B'}. \tag{8}$$

Because the loading at point B is positive and the loading at point B' is zero (no blade), the front loading near the tip of an aft-swept blade will be higher than that of a forward swept blade:

$$\lambda_A = \lambda_{A'} + \lambda_B > \lambda_{A'}. \tag{9}$$

Similarly, it can be deduced that the front loading near the hub of an aft-swept blade will be lower than that of a forward swept blade.

For axial-to-radial parts of centrifugal compressors, illustration of loading is shown in Figure 17b. The spanwise equivalent equation and the spanwise gradient of blade loading are deduced as follows:

$$F_n + \frac{V_t^2}{r} \cos \delta = V_m \frac{\partial V_n}{\partial m} + V_n \frac{\partial V_n}{\partial n} + \frac{1}{\rho} \frac{\partial p}{\partial n} \tag{10}$$

$$\frac{\partial \lambda}{\partial n} = -\rho \frac{V_{t,s}^2 - V_{t,p}^2}{r} \cos \delta, \tag{11}$$

where m and n are streamwise and spanwise coordinates, and δ is the streamline slope angle. The loading gradient near the hub remains constant with changing sweep angle. Thus, similar conclusions can be drawn for the hub front loading. The loading gradient near the tip increases when sweeping forward the blade, because the incoming flow has a lower tangential velocity at upstream positions. Comparing Equations (3) and (4):

$$\lambda_A - \lambda_B = \int_{r_B}^{r_A} \frac{\partial \lambda}{\partial r} dr = \int_{r_{B'}}^{r_{A'}} \frac{\partial \lambda}{\partial r} dr - \Delta\lambda = \lambda_{A'} - \lambda_{B'} - \Delta\lambda. \tag{12}$$

It shows that the unloading effect of forward sweep near the tip has been hindered by the altered incoming flow condition. Limited change in tip loading is therefore expected:

$$\lambda_A = \lambda_{A'} + \lambda_B - \Delta\lambda \approx \lambda_{A'}. \tag{13}$$

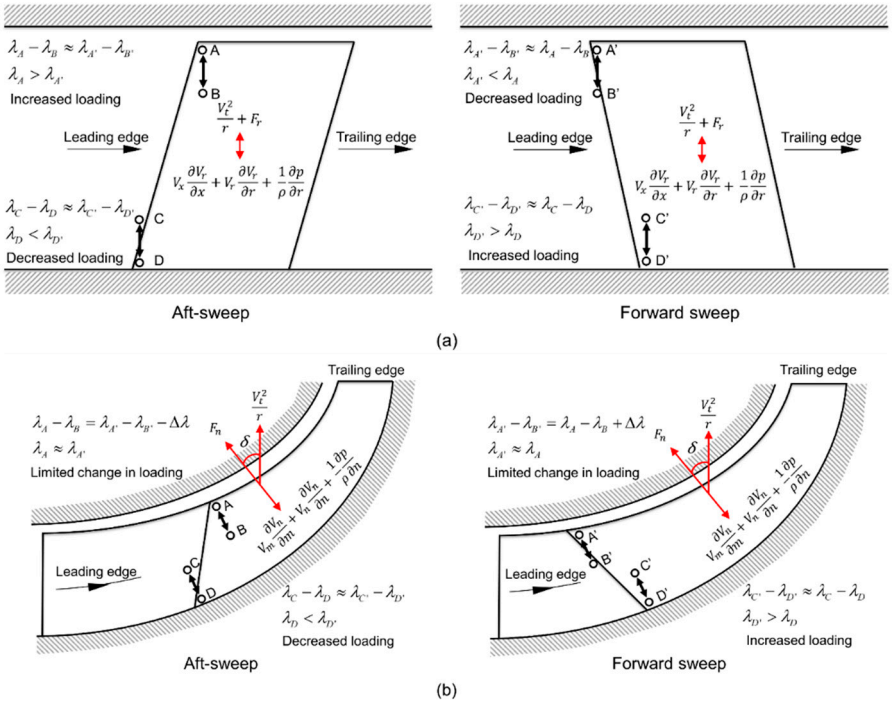

Figure 17. Understanding sweep effects on the front loading of (**a**) axial compressors and (**b**) centrifugal compressors through loading definition.

The above equivalent explanations support most of the loading changes in Figure 15 except for the hub loading of splitter I. Since all blades sweep together in the current investigation, the upstream swept blades will influence downstream blades. When increasing the sweep angle, the increased hub front loading of the main blade leads to a thickened boundary layer or even flow separations near the pressure surface, which reduces the channel diffusion ratio and decreases hub incidence of splitter I. Its hub loading is therefore decreased.

5.2. Effect on the Shock Structure

In the datum case, a weak passage shock followed by the tip leakage vortex trajectory can be observed from Figure 18. In the OSA and the MSA case, both the shock and the downstream low-momentum flow region are eliminated. The decreased shock strength is owned to both the extended chord length and the unloading effect of the tip section. Since the definition of sweep keeps the blade angle distribution along the relative chord length unchanged, the extended chord length by the enlarged sweep angle will decrease the blade turning at the front part, and thus the shock strength is decreased. Moreover, the unloading effect of the enlarged sweep angle lowered the streamwise pressure rise by the shock, which also inclines to decrease the shock strength. The reduced shock strength contributes to the reduced local shock loss. However, referring to Figure 11, the reduced shock loss in the front part is relatively limited compared to that in the rear part of the impeller.

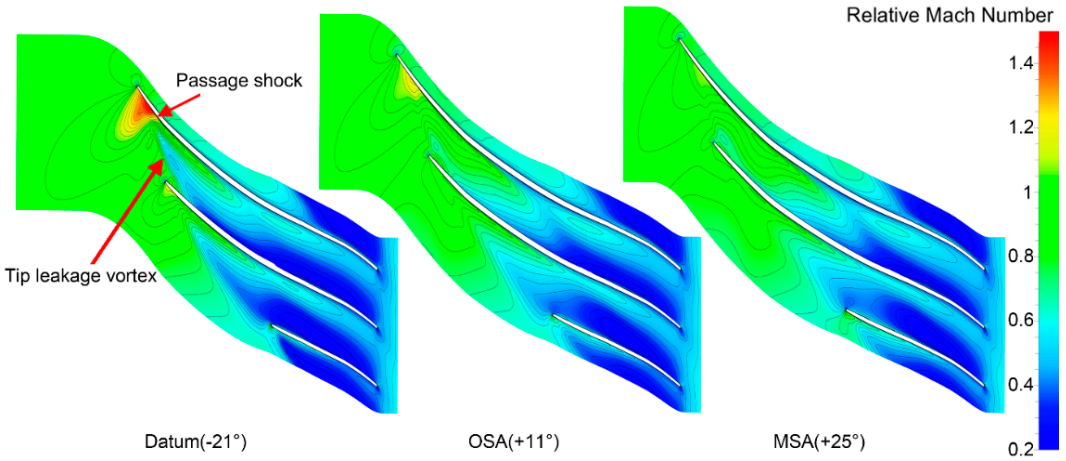

Figure 18. Contours of relative Mach number at 95% span.

5.3. Effect on the Tip Leakage Vortex

Limiting streamlines with static pressure contour are presented in Figure 19. In the datum case, the thickened boundary layer downstream the shock radially migrates to the tip, increasing the blockage. The shock is therefore pushed further upstream and away from casing, resulting in a stronger shock effect and thus the shock-boundary layer interaction. In the OSA and the MSA case, the radial migrating process has been successfully suppressed. The forward sweep restricts the radial migration of low-momentum flow by two mechanisms. Firstly, the reduced shock strength results in a thinner boundary layer and decreases the amount of boundary layer low-momentum flow. Secondly, the leading edge near the tip starts earlier when sweeping forward. The high-pressure region of the tip section is moved more upstream, which increases the tip pressure and counteracts with the outward spanwise pressure gradient.

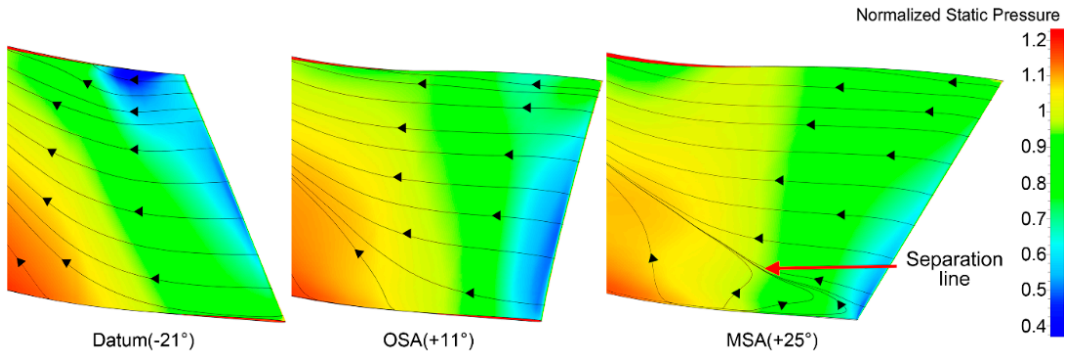

Figure 19. Contours of static pressure and streamlines on the suction surface of main blade.

As observed in the datum case in Figure 20, the radially migrated flow of the boundary layer mixes with the tip leakage flow, forming the tip leakage vortex. The vortex is gradually dissipated, and finally joins the downstream wake region in the passage between main blade and splitter I. However, in the OSA case, the boundary layer flow and the tip leakage flow decouple with each other due to the suppressed radial migration of low-momentum flow. The tip leakage vortex is therefore restrained, and the downstream wake loss is decreased, which corresponds to the gradual efficiency increase from Section I to the exit as illustrated in Figure 11. At impeller exit, the improved efficiency near the casing between main blade and splitter I is captured in Figure 12b.

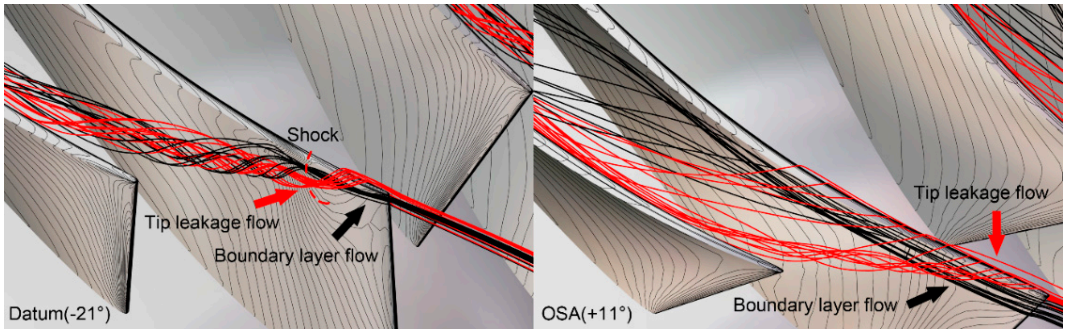

Figure 20. 3D tip streamlines and static pressure isolines on main blade and splitter I.

In the datum case, a tip leakage vortex is also observed near splitter II, as presented in Figure 21. The vortex is formed from the interaction between the incoming main flow and the tip leakage flow. The high momentum main flow immediately separates from the suction surface due to the large incidence at splitter II, which is induced by the slip effect. The tip leakage flow across the tip gap of splitter II is driven by the pressure difference (or tip loading). Then the vortex is gradually dissipated, and finally joins the downstream wake region in the passage between main blade and splitter II. In the OSA case, because of the unloading effect of splitter sweep, both the main flow separation and the tip leakage flow have been constrained. Hence, the tip leakage vortex and the downstream wake loss have been controlled. The efficiency then gradually increases from Section II to the exit with a steeper slope than that from Section I to Section II, as illustrated in Figure 11. It is also confirmed in Figure 12b that the reduced wake loss improved the impeller exit efficiency near the casing between main blade and splitter II. To control flow separations at splitter tip, an alternative choice of splitter sweep is the splitter tip re-cambering, where the incidence is controlled by readjusting the inlet blade angle [39].

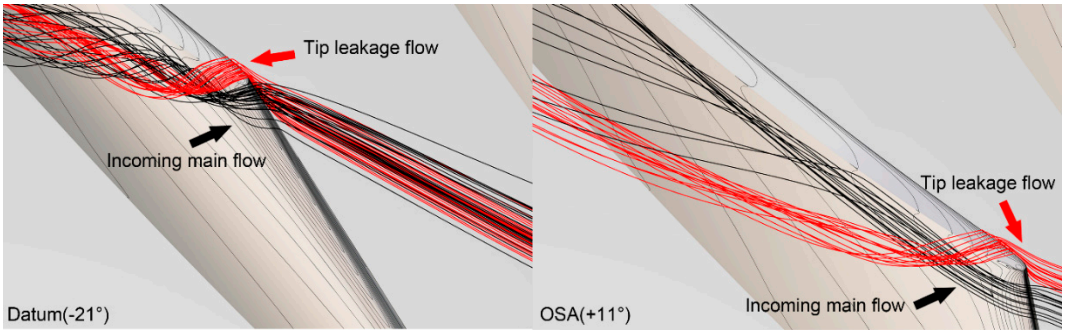

Figure 21. 3D tip streamlines and static pressure isolines on splitter II.

5.4. Effect on the Flow Separation

As illustrated in Figure 22, flow separation occurs near the hub of main blade when the sweep angle has been increased to an extremely large value. The flow separation is caused by the sweep effect on the front loading, where the hub incidence and the adverse pressure gradient will be intensified when sweeping forward. The induced flow separation near the hub will introduce extra loss that corresponds to the enhanced loss at Section I, as discussed in Figures 11 and 12a. To control such separations near the hub, an intuitive way is to adopt an aft-swept leading edge [23], but it will enhance the loss near the casing, as discussed before. A combination of hub re-cambering and forward sweep is advantageous near the hub and shroud, resulting in a hub-side end-bend feature [40].

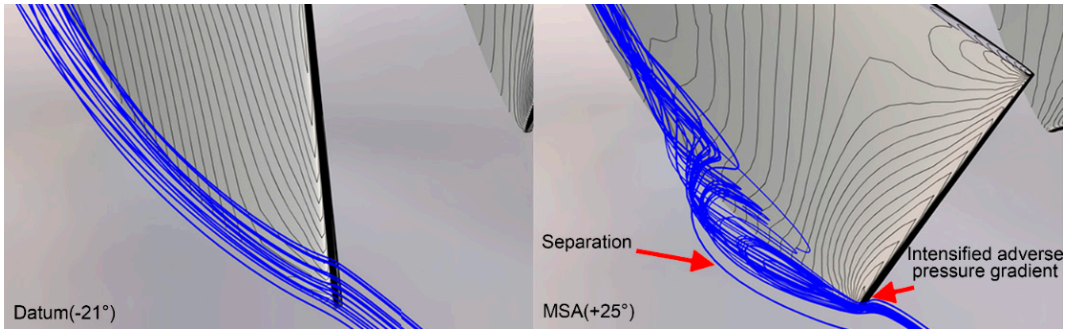

Figure 22. 3D hub streamlines and static pressure isolines on main blade and splitter I.

5.5. Causal Link between Aerodynamics Effects and Compressor Efficiency

The cause–effect relationship between the performance improvement and the aerodynamic effects of sweep is illustrated in Figure 23. The essential aerodynamic effect of sweep is the spanwise redistribution of the front loading, subsequently resulting in effects on the shock structure, the tip leakage vortex, and the flow separation. When the blade is forward-swept, the reduced tip loading leads to the suppressed shock strength and the suppressed tip leakage vortex, which improves the efficiency near the tip. When the blade is aft-swept, the decreased hub loading leads to suppressed flow separation, which improves the efficiency near the hub.

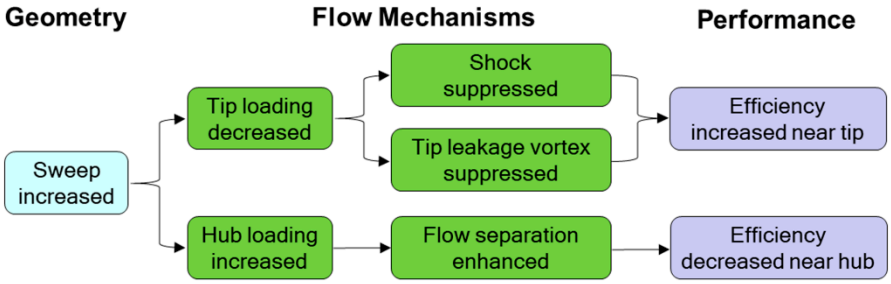

Figure 23. Illustration of sweep mechanism.

Hence, it is the delicate balance between controlling the shock and the tip leakage vortex near the tip, as well as controlling the near-hub flow separation, that achieves the best efficiency. This is the underlying mechanism for the optimal sweep angle. Since the designed spanwise front loading distribution is usually different, it is deduced that forward sweep is efficient in cases whose front loading near the tip is heavy, while aft sweep raises the efficiency in cases that have high loading near the hub.

For transonic centrifugal impellers, the tip section is usually heavily loaded due to the existence of shock. Thus, a forward swept main blade is expected to be beneficial. According to the literature survey in Table 2, an optimal sweep angle around +10° is found based on several transonic centrifugal impellers cases. With the increasing pressure ratio, the effect of sweep on compressor efficiency rises as well.

Table 2. Optimal sweep design in transonic impellers.

π_d	Sweep Range (°)	η Range	Optimal Sweep (°)	References
3.0	−25 to +25	1.2%	+11	Current study
3.7	−5 to +10	1.5%	+10	Hazby and Xu [25]
5.9	0 to +20	3.7%	+10	Liu et al. [41]
5.7	−10 to +10	3.9%	+8	He and Zheng [39]

6. Conclusions

Mechanisms by which the sweep feature affects the performance of a transonic centrifugal compressor impeller with twin splitters have been discussed through numerical method. Sweep is defined as scaling up or down the shroud chord while keeping the blade angle and the thickness distribution along the relative chord length unchanged. The variation range of the sweep angle has been set at -25° to $+25^\circ$. Several conclusions can be drawn, as follows:

1. Sweep feature has a great impact on the choke mass flow rate, efficiency and pressure ratio of the impeller. Its effect on compressor efficiency will be stronger if the centrifugal compressor has a higher pressure ratio or a higher front loading.
2. Sweep influences the flowfields through the effects on the front loading, the shock structure, the tip leakage vortex, and the flow separation. On the shroud section, forward sweep tends to restrict the front loading, the shock strength and the tip leakage vortex, which reduces the loss near the casing. On the hub section, aft sweep suppresses the front loading and the flow separation, which reduces the loss near the hub.
3. The mechanism for the optimal sweep angle is deduced to be a trade-off between the effects of reduced tip leakage loss and the enhanced hub endwall loss. Because the spanwise front loading distribution varies in different cases, the optimal sweep angle, which in the investigated case occurs near $+11^\circ$, will be different in other cases. Forward sweep is expected to be more efficient in heavy tip loading cases, while in heavy hub loading ones aft sweep has the potential to increase efficiency.

Acknowledgments: This research was supported by the National Natural Science Foundation of China (Grant No. 51176087). The authors would like to thank Andrew Heyes from the University of Strathclyde for the enlightening comments and discussions. Special thanks to the anonymous reviewers who offered valuable suggestions and comments for improving the manuscript.

Author Contributions: Xiao He acquired the data and wrote the paper; Xinqian Zheng revised the paper.

Conflicts of Interest: The authors declare no conflict of interest.

Nomenclature

b	blade height
c_p	specific heat capacity at constant pressure
F	blade force
h	enthalpy
m	mass flow rate
M	normalized distance along the meridional curve
MSA	case with the maximum sweep angle
n	distance in the spanwise direction
N	normalized distance in the spanwise direction
OSA	case with the optimal sweep angle
p	pressure
r	distance in the radial direction
s	entropy
T	temperature
U	blade speed
V	absolute velocity
y^+	normalized wall distance
Z	number of blades
γ	ratio of specific heat capacities
δ	streamline slope angle
η	isentropic efficiency
θ	tangential angle

λ	blade loading
π	total pressure ratio
ρ	density

Subscripts:

1	impeller inlet
2	impeller exit
c	choke condition
d	design condition
m	meridional component
p	pressure side
r	radial component
s	suction side
t	tangential component

Definitions of non-dimensional parameters:

ϕ	flow coefficient $\frac{m}{4\rho_1 U_2 r_2^2}$
ψ	pressure coefficient $\frac{h_{2s}-h_1}{U_2^2}$
N_s	specific speed $\frac{2\varphi^{1/2}}{\psi^{3/4}}$

Appendix A. Correlation between the Sweep Angle and the Induced Inlet Lean Angle

The current sweep definition will introduce an extra inlet lean angle. The correlation between these two angles is analyzed here.

Considering to extend the tip of the leading edge along the chord direction while maintaining the rest part unchanged, the shroud inlet tangential position of the extended case (θ_{E1}) is deduced as follows:

$$\theta_{E1} = \frac{r_{1t} - r_{1h}}{r_{1t}} \tan\alpha_S \tan\beta_{1t} + \theta_1, \tag{A1}$$

where r_{1h} and r_{1t} are the inlet hub and tip radius, and α_S, β_{1t}, and θ_1 are the defined sweep angle, the inlet tip blade angle and the shroud inlet tangential position of the datum case, respectively. The difference between r_{1h} and r_{1t} is the inlet blade height (b_1).

Considering the current sweep definition by scaling up or down the shroud chord, the scale factor can be estimated with the assumption that the inlet blade shape is linear and its slope is $\tan\beta_{1t}$:

$$\frac{\theta_{S1} - \theta_2}{\theta_1 - \theta_2} = 1 + \frac{r_{1t} - r_{1h}}{c_s} \frac{\tan\alpha_S}{\cos\beta_{1t}}, \tag{A2}$$

where c_s is the shroud chord length, θ_{S1} is the shroud inlet tangential position of the swept case, and θ_2 is the shroud exit tangential position of the datum case. The difference between θ_1 and θ_2 is often referred to the wrap angle. θ_{S1} is then obtained as follows:

$$\theta_{S1} = \frac{r_{1t} - r_{1h}}{c_s} \frac{\tan\alpha_S}{\cos\beta_{1t}} (\theta_1 - \theta_2) + \theta_1. \tag{A3}$$

The difference between θ_{E1} and θ_{S1} is defined as the induced inlet lean angle (θ_{L1}). A positive value of it indicates that the blade has leaned to the rotating direction, and the opposite to the counter-rotating direction.

$$\begin{aligned} \theta_{L1} &= \theta_{S1} - \theta_{E1} \\ &= (1 - \frac{r_{1h}}{r_{1t}})[\frac{r_{1t}(\theta_1 - \theta_2) - c_s \sin\beta_{1t}}{c_s \cos\beta_{1t}}] \tan\alpha_S. \\ &\approx (1 - \frac{r_{1h}}{r_{1t}})[\frac{r_{1t}(\theta_1 - \theta_2) - c_s \sin\beta_{1t}}{c_s \cos\beta_{1t}}]\alpha_S \end{aligned} \tag{A4}$$

For the current case, the ratio of θ_{L1} over α_S is calculated to be -13%, which indicates that an increase in sweep angle will result in a small negative inlet lean angle.

References

1. Wang, Y.; Shi, D.; Zhang, D.; Xie, Y. Investigation on Unsteady Flow Characteristics of a SCO2 Centrifugal Compressor. *Appl. Sci.* **2017**, *74*, 310. [CrossRef]
2. Albusaidi, W.; Pilidis, P. An Iterative Method to Derive the Equivalent Centrifugal Compressor Performance at Various Operating Conditions: Part II: Modeling of Gas Properties Impact. *Energies* **2015**, *8*, 8516–8536. [CrossRef]
3. Hosseini, M.; Sun, Z.; He, X.; Zheng, X. Effects of Radial Gap Ratio between Impeller and Vaned Diffuser on Performance of Centrifugal Compressors. *Appl. Sci.* **2017**, *7*, 728. [CrossRef]
4. Ebrahimi, M.; Huang, Q.; He, X.; Zheng, X. Effects of Variable Diffuser Vanes on Performance of a Centrifugal Compressor with Pressure Ratio of 8.0. *Energies* **2017**, *10*, 682. [CrossRef]
5. Krain, H. Review of Centrifugal Compressor's Application and Development. *J. Turbomach.* **2005**, *127*, 25–34. [CrossRef]
6. Lin, Y.; Zheng, X.; Jin, L.; Tamaki, H.; Kawakubo, T. A Novel Experimental Method to Evaluate the Impact of the Volute's Asymmetry on the Performance of a High Pressure Ratio Turbocharger Compressor. *Sci. China Technol. Sci.* **2012**, *55*, 1695–1700. [CrossRef]
7. Zheng, X.; Lin, Y.; Gan, B.; Zhuge, W.; Zhang, Y. Effects of Reynolds Number on the Performance of a High Pressure-Ratio Turbocharger Compressor. *Sci. China Technol. Sci.* **2013**, *56*, 1361–1369. [CrossRef]
8. Cumpsty, N.A. *Compressor Aerodynamics*; Longman Scientific and Technical: Harlow, UK, 1989; pp. 249–254.
9. Ibaraki, S.; Matsuo, T.; Kuma, H.; Sumida, K.; Suita, T. Aerodynamics of a Transonic Centrifugal Compressor Impeller. *J. Turbomach.* **2003**, *125*, 346–351. [CrossRef]
10. Denton, J.D.; Xu, L. The Exploitation of Three-Dimensional Flow in Turbomachinery Design. *Proc. Inst. Mech. Eng. C* **1998**, *213*, 125–137. [CrossRef]
11. Zheng, X.; Li, Z. Blade-End Treatment to Improve the Performance of Axial Compressors: An Overview. *Prog. Aerosp. Sci.* **2017**, *88*, 1–14. [CrossRef]
12. Vad, J. Aerodynamic Effects of Blade Sweep and Skew in Low-Speed Axial Flow Rotors at the Design Flow Rate: An Overview. *Proc. Inst. Mech. Eng. A* **2008**, *222*, 69–85. [CrossRef]
13. Okui, H.; Verstraete, T.; Van den Braembussche, R.A.; Alsalihi, Z. Three-Dimensional Design and Optimization of a Transonic Rotor in Axial Flow Compressors. *J. Turbomach.* **2013**, *135*, 031009. [CrossRef]
14. Vad, J. Forward Blade Sweep Applied to Low-Speed Axial Fan Rotors of Controlled Vortex Design: An overview. *J. Eng. Gas Turbines Power* **2013**, *135*, 012601. [CrossRef]
15. Ilikan, A.N.; Ayder, E. Influence of the Sweep Stacking on the Performance of an Axial Fan. *J. Turbomach.* **2015**, *137*, 061004. [CrossRef]
16. Hah, C.; Puterbaugh, S.L.; Wadia, A.R. Control of Shock Structure and Secondary Flowfield inside Transonic Compressor Rotors through Aerodynamic Sweep. In Proceedings of the International Gas Turbine and Aeroengine Congress and Exhibition, Stockholm, Sweden, 2–5 June 1998.
17. Benini, E.; Biollo, R. Aerodynamics of Swept and Leaned Transonic Compressor-Rotors. *Appl. Energy* **2007**, *84*, 1012–1027. [CrossRef]
18. Cui, W.; Xiang, X.; Zhao, Q.; Xu, J. The Effect of Sweep on Flowfields of a Highly Loaded Transonic Rotor. *Aerosp. Sci. Technol.* **2016**, *58*, 71–81. [CrossRef]
19. Denton, J.D.; Xu, L. The Effects of Lean and Sweep on Transonic Fan Performance. In Proceedings of the ASME Turbo Expo 2002: Power for Land, Sea, and Air, Amsterdam, The Netherlands, 3–6 June 2002.
20. Hah, C.; Shin, H.W. Study of Near-Stall Flow Behavior in a Modern Transonic Fan with Compound Sweep. *J. Fluids Eng.* **2012**, *134*, 071101. [CrossRef]
21. Ji, L.; Chen, J.; Lin, F. Review and Understanding on Sweep in Axial Compressor Design. In Proceedings of the ASME Turbo Expo 2005: Power for Land, Sea, and Air, Reno, NV, USA, 6–9 June 2005.
22. Palmer, D.L.; Waterman, W.F. Design and Development of an Advanced Two-Stage Centrifugal Compressor. *J. Turbomach.* **1995**, *117*, 205–212. [CrossRef]
23. Krain, H.; Hoffmann, B. Flow Study of a Redesigned High-Pressure-Ratio Centrifugal Compressor. *J. Propul. Power* **2008**, *24*, 1117–1123. [CrossRef]
24. Hazby, H.; Casey, M.; Numakura, R.; Tamaki, H. A Transonic Mixed Flow Compressor for an Extreme Duty. *J. Turbomach.* **2015**, *137*, 051010. [CrossRef]

25. Hazby, H.R.; Xu, L. Effects of Leading Edge Sweep on the Performance of a Centrifugal Impeller. In Proceedings of the 18th ISABE (International Symposium on Air Breathing Engines) Conference, Beijing, China, 2–7 September 2007.
26. Erdmenger, R.R.; Michelassi, V. Impact of Main and Splitter Blade Leading Edge Contour on the Performance of High Pressure Ratio Centrifugal Compressors. In Proceedings of the ASME Turbo Expo 2014: Turbine Technical Conference and Exposition, Düsseldorf, Germany, 16–20 June 2014.
27. Hazby, H.R.; Xu, L. Numerical Investigation of the Effects of Leading Edge Sweep in a Small Transonic Impeller. In Proceedings of the Eighth European Conference on Turbomachinery Fluid Dynamics and Thermodynamics, Graz, Austria, 23–27 March 2009; pp. 459–467.
28. Hazby, H.; Woods, I.; Casey, M.; Numakura, R.; Tamaki, H. Effects of Blade Deformation on the Performance of a High Flow Coefficient Mixed Flow Impeller. *J. Turbomach.* **2015**, *137*, 121005. [CrossRef]
29. He, X.; Zheng, X. Mechanisms of Lean on the Performance of Transonic Centrifugal Compressor Impellers. *J. Propul. Power* **2016**, *32*, 1220–1229. [CrossRef]
30. Casey, M. Thematic Area 6: Best Practice Advice for Turbomachinery Internal Flows. *QNET- CFD Netw. Newsl.* **2004**, *24*, 40–46.
31. Denton, J.D. Some Limitations of Turbomachinery CFD. In Proceedings of the ASME Turbo Expo 2010: Power for Land, Sea, and Air, Glasgow, UK, 14–18 June 2010.
32. Mangani, L.; Casartelli, E.; Mauri, S. Assessment of Various Turbulence Models in a High Pressure Ratio Centrifugal Compressor with an Object Oriented CFD Code. *J. Turbomach.* **2012**, *134*, 061033. [CrossRef]
33. Gibson, L.; Galloway, L.; Kim, S.; Spence, S. Assessment of Turbulence Model Predictions for a Centrifugal Compressor Simulation. *J. Glob. Power Propul. Soc.* **2017**, *1*, 142–156. [CrossRef]
34. Spalart, P.; Allmaras, S. A One-Equation Turbulence Model for Aerodynamic Flows. In Proceedings of the 30th Aerospace Sciences Meenting and Exhibt, Reno, NV, USA, 6–9 January 1992.
35. Casey, M.; Rusch, D. The Matching of a Vaned Diffuser with a Radial Compressor Impeller and Its Effect on the Stage Performance. *J. Turbomach.* **2014**, *136*, 121004. [CrossRef]
36. Eisenlohr, G.; Krain, H.; Richter, F.A.; Tiede, V. Investigations of the Flow through a High Pressure Ratio Centrifugal Impeller. In Proceedings of the ASME Turbo Expo 2002: Power for Land, Sea, and Air, Amsterdam, The Netherlands, 3–6 June 2002.
37. Krain, H.; Hoffmann, B.; Pak, H. Aerodynamics of a Centrifugal Compressor Impeller with Transonic Inlet Conditions. In Proceedings of the ASME 1995 International Gas Turbine and Aeroengine Congress and Exposition, Houston, TX, USA, 5–8 June 1995.
38. Denton, J.D. The 1993 IGTI Scholar Lecture: Loss Mechanisms in Turbomachines. *J. Turbomach.* **1993**, *115*, 621–656. [CrossRef]
39. Came, P.M.; Robinson, C.J. Centrifugal Compressor Design. *Proc. Inst. Mech. Eng. C* **1998**, *213*, 139–155. [CrossRef]
40. He, X.; Zheng, X. Performance Improvement of Transonic Centrifugal Compressors by Optimization of Complex Three-Dimensional Features. *Proc. Inst. Mech. Eng. G* **2016**. [CrossRef]
41. Liu, Y.; Cui, Q.; Zheng, X.; Guo, L. Numerical Investigation of Flow Field for Transonic Centrifugal Compressor with Blade Leading Edge Forward Sweep. *J. Auto Saf. Energy* **2015**, *6*, 392–398. (In Chinese)